The Cryosphere Discuss., doi:10.5194/tc-2016-168, 2016
Manuscript under review for journal The Cryosphere
Published: 30 August 2016

Mapping snow depth within a tundra ecosystem using multiscale observations and Bayesian methods

Haruko M. Wainwright
hmwainwright@lbl.gov
Earth Sciences Division, Lawrence Berkeley National Laboratory
1 Cyclotron Road, MS 74R-316C, Berkeley, CA 94720-8126

Anna K. Liljedahl
akliljedahl@alaska.edu
Water & Environmental Research Center
University of Alaska Fairbanks
306 Tanana Loop, Fairbanks, AK 99775-5860, USA

Baptiste Dafflon
bdafflon@lbl.gov
Earth Sciences Division, Lawrence Berkeley National Laboratory
1 Cyclotron Road, MS 74R-316C, Berkeley, CA 94720-8126

Craig Ulrich
CUlrich@lbl.gov
Earth Sciences Division, Lawrence Berkeley National Laboratory
1 Cyclotron Road, MS 74R-316C, Berkeley, CA 94720-8126

The Cryosphere Discuss., doi:10.5194/tc-2016-168, 2016
Manuscript under review for journal The Cryosphere
Published: 30 August 2016

John E. Peterson
jepeterson@lbl.gov
Earth Sciences Division, Lawrence Berkeley National Laboratory
1 Cyclotron Road, MS 74R-316C, Berkeley, CA 94720-8126

Susan S. Hubbard
sshubbard@lbl.gov
Earth Sciences Division, Lawrence Berkeley National Laboratory
1 Cyclotron Road, MS 74R-316C, Berkeley, CA 94720-8126

The Cryosphere Discuss., doi:10.5194/tc-2016-168, 2016
Manuscript under review for journal The Cryosphere
Published: 30 August 2016

Abstract

This paper compares and integrates different strategies to characterize the variability of end-of-winter snow depth and its relationship to topography in ice-wedge polygon tundra of Arctic Alaska. Snow depth was measured using *in situ* snow depth probes, and estimated using ground penetrating radar (GPR) surveys and the Photogrammetric Detection and Ranging (PhoDAR) technique with an unmanned aerial system (UAS). We found that GPR data provided high-precision estimates of snow depth (RMSE = 2.9 cm), with a spatial sampling of 10 cm along transects. UAS-based approaches provided snow depth estimates in a less laborious manner compared to GPR and probing while yielding a high precision (RMSE = 6.0 cm) and a fine spatial sampling (4 cm by 4 cm). We then investigated the spatial variability of snow depth and its correlation to micro- and macrotopography using the snow-free LiDAR digital elevation map (DEM) and the wavelet approach. We found that the end-of-winter snow depth was highly variable over short (several meter) distances, and the variability was correlated with microtopography. Microtopographic lows (i.e., troughs and centers of low-centered polygons) were filled in with snow, which resulted in a smooth and even snow surface following macrotopography. We developed and implemented a Bayesian approach to integrate the snow-free LiDAR DEM and multi-scale measurements (probe and GPR) as well as the topographic correlation for estimating snow depth over the landscape. Our approach led to high precision estimates of snow depth (RMSE = 6.0 cm), at 0.5-meter resolution and over the LiDAR domain (750 m by 700 m).

The Cryosphere Discuss., doi:10.5194/tc-2016-168, 2016
Manuscript under review for journal The Cryosphere
Published: 30 August 2016

1. Introduction

Snow plays a critical role in ecosystem functioning of the Arctic tundra environment through its impacts on soil hydrothermal processes and energy exchange (e.g., Callaghan et al., 2011). Snow insulates the ground from intense cold during the Arctic winter, limiting the heat transfer between the air and the ground (Zhang, 2005). Snow depth affects active layer and permafrost temperatures throughout the year (Gamon et al., 2012; Stieglitz et al., 2003), and increased snow depth has resulted in permafrost degradation (Osterkamp, 2007). Snow's insulating capacity enhances conditions for active soil microbial processes and CO_2/CH_4 production during winter (Nobrega and Grogan, 2007; Schimel et al., 2004; Clein and Schimel, 1995; Jansson and Taş, 2014; Zona et al., 2016). In addition, snow serves as an important water source to tundra ecosystems during the growing season, and therefore has a large impact on biological processes via hydrology. Snowmelt water can lead to extensive inundation of low-gradient tundra and large runoff events in early summer (Bowling et al., 2003; Kane et al., 1991; Liljedahl et al., 2016). Since soil biogeochemistry and vegetation are controlled by soil moisture (Sjögersten et al., 2006; Wainwright et al., 2015), the amount of snow affects ecosystem functioning throughout the season.

In order to investigate controls of snow on ecosystem properties, high resolution estimates of snow are needed over large spatial regions. This is especially true in ice-wedge polygon tundra, which dominates a large portion of the high Arctic (Zona et al., 2011). Polygon evolution – caused by successive freezing, cracking and thawing of soil and ice and associated movement of soil – leads to *microtopography*, where the ground surface elevation can vary significantly over lateral length distances of several meters (e.g., Brown, 1967; MacKay, 2000). This microtopography leads to dramatically variable snow depth across short distances. Liljedahl et al. (2016) found that the differential snow distribution increased the partitioning of snowmelt water into runoff, leading to less water stored on the tundra landscape. Gamon et al. (2012) reported that snow depth heterogeneity results in differential thawing and active layer thickness variability. In addition, there are large-scale spatial variability in ground surface elevation, or *macrotopography*, which can vary over lateral distances of several hundred meters to kilometers; macrotopography is often associated with drained thaw lake basins or drainage features (Hinkel et al., 2003). To account for the effect of such multiscale terrain heterogeneities on hydrology and ecosystem functioning, the snow representation of the Arctic tundra needs to be refined, especially by bridging from finer geographical scales (sub-meter) to large areal coverage (several hundred meters to kilometers).

In the tundra environment, snow depth characterization has been limited to ground-based point (probe) measurements (Benson and Sturm, 1993; Dvornikov et al., 2015). Recently, there have been several new techniques for estimating snow depth in high resolution, and in a non-invasive and spatially extensive manner. Ground-penetrating radar (GPR) has been widely used to characterize snow cover in alpine, arctic and glacier environments (e.g., Harper and Bradford, 2003; Machguth et al., 2006; Gusmeroli and Grosse, 2012; Gusmeroli et al., 2014). GPR measures the radar reflection from the snow and ground surface, which can be used to estimate show depth. GPR can be collected by foot, snowmobile or airborne methods. In addition, Light Detection and Ranging (LiDAR) and Photogrammetric Detection and Ranging (PhoDAR) airborne methods have recently been used to estimate snow depth at site or regional scales (e.g., Deems et al., 2013; Harpold et al., 2014; Nolan et al., 2015). Both techniques measure the snow surface elevation, using laser in LiDAR, and the structure-from-motion (SfM) algorithm in PhoDAR, which allows us to estimate snow depth by subtracting the snow-free elevation. While the potential of those advanced methods for providing information about snow variability has been documented, they have not been used extensively for characterizing the variability of snow depth in ice-wedge polygonal tundra.

Such indirect geophysical methods are, however, known to have increased uncertainty relative to direct measurements (here ground-based probe measurements) (e.g., Hubbard and Rubin, 2005). For example, the snow depth estimates obtained using GPR can be affected by uncertainty associated with radar velocity, which depends on snow density (Harper and Bradford, 2003). In the environments with complex terrain such as ice-wedge polygonal tundra, GPR-based snow estimates could also be influenced by the errors stemming from radar positioning and raypath assumptions. The airborne LiDAR/PhoDAR-based methods are subject to the errors associated with georeferencing, processing and calibration (e.g., Deems et al., 2013; Nolan et al., 2015). The accuracy of the airborne methods is usually several tens of centimeters, which is lower than the centimeter accuracy of the probe measurements.

Integrating different types of snow measurements can take advantage of the strengths of various techniques while minimizing the limitations stemming from using a single method. Bayesian approaches have proven to be useful for integrating multiscale multi-type datasets to estimate spatially heterogeneous terrestrial system parameters in a manner that honors method-specific uncertainty (e.g., Wikle et al., 2001; Wainwright et al., 2014; 2016). Bayesian methods also permit systematic incorporation of expert knowledge or process-specific information, such as the

The Cryosphere Discuss., doi:10.5194/tc-2016-168, 2016
Manuscript under review for journal The Cryosphere
Published: 30 August 2016

relationships between datasets and parameters. In particular, snow depth is known to be affected by topography and wind direction (e.g., Benson and Sturm, 1993; Anderson et al., 2014; Dvornikov et al., 2015). To our knowledge, such integration methods have not been developed to estimate end-of-winter snow variability using multiple types of datasets.

The primary objectives of this study are to (1) compare point probe, GPR and UAS approaches for characterizing snow depth, and the associated resolution and accuracy of the GPR and UAS methods; (2) characterize the spatial heterogeneity of end-of-winter snow depth in ice-wedge polygonal tundra landscape; (3) explore the relationship between snow depth and topography; and (4) develop a Bayesian method to integrate multiscale multi-type data to estimate snow depth over the LiDAR domain. In Section 2, we describe our site and datasets, including point probes, GPR and UAS-based PhoDAR. In Section 3, we present the methodology to analyze the indirect snow depth measurements from GPR and PhoDAR as well as to evaluate the heterogeneity of snow depth in relation to both microtopography (i.e., ice-wedge polygons) and macrotopography (i.e., large-scale gradient, drained thaw lake basins and interstitial upland tundra). We then develop a Bayesian geostatistical approach to integrate the multiscale datasets to estimate snow depth over the LiDAR domain. The snow measurement and estimation results are presented in Section 4 and discussed in Section 5.

The Cryosphere Discuss., doi:10.5194/tc-2016-168, 2016
Manuscript under review for journal The Cryosphere
Published: 30 August 2016

2. Data and Site Descriptions

2.1. Study Site

Snow survey data were collected within a study site (approximately 750 m by 700 m) located on the Barrow Environmental Observatory near Barrow, Alaska, as part of the Department of Energy's Next-Generation Ecosystem Experiment Arctic project (Figure 1). Mean annual air temperature at the Barrow site is –11.3°C and mean annual precipitation is 173 mm (Liljedahl et al., 2011). Snowmelt usually ends in early to mid-June. The wind direction is predominantly from east to west throughout the year. Ice-wedge polygons are prevalent in the region, including low-centered polygons in drained thaw lake basins and high-centered polygons with well-developed troughs in the upland tundra (Hinkel et al., 2003; Wainwright et al., 2015). The dominant plants are mosses (*Dicranum elongatum*, *Sphagnum*), lichens and vascular plants (such as *Carex aquatilis*); plant distribution at the site is governed by surface moisture variability (e.g., Hinkel et al., 2003; Zona et al., 2011). There are no shrubs or tall woody plants that are known to affect snow depth (Sturm et al., 2005; Dvornikov et al., 2015).

Three transects and four representative plots were chosen within the study site to explore snow variability and its relationship to topography (Figure 1). Typical for low-gradient tundra terrain, ice-wedge polygon microtopographic variations are superimposed on macrotopographic trends at the study site. The elevation is higher in the center of the domain (interstitial upland tundra) and lower near the drainage features in the south. The elevation is also relatively lower in the drained thaw lake basins (DTLB) region, which is located in the northeastern and northwestern edges of the study site. The four intensive plots (A-D), each 160m x 160m, were chosen to represent specific polygon types or macrotopographic positions within the study area. The three parallel

The Cryosphere Discuss., doi:10.5194/tc-2016-168, 2016
Manuscript under review for journal The Cryosphere
Published: 30 August 2016

transects, each ~500m long, were designed to traverse multiple polygon types in a continuous fashion (Hubbard et al., 2013).

2.2. Datasets

Airborne LiDAR data were collected at the site on October 4th, 2005, providing a high-resolution digital elevation map (DEM) of the snow-free ground at 0.5 m by 0.5 m resolution (Hubbard et al., 2013). The DEM effectively resolved both micro- and macrotopography at the study site (Figure 1). To evaluate the accuracy of the airborne DEM, we measured the ground surface elevation in September 2011 using a high-precision centimeter-grade RTK Differential GPS (DGPS) system. The root mean square error of the LiDAR DEM compared to GPS was 6.08 cm.

The majority of the snow depth data was collected on May 6–12, 2012, during which no snowfall occurred and little change in snow depth was observed. Snow depth was measured in the four intensive study plots and along three transect lines (Figure 1). Two sets of snow depth measurements using a snow probe were collected. The 'fine-grid' dataset was aimed to characterize the fine-scale heterogeneity by ~7200 snow depth point measurements (every ~0.3 m along transects with a 4 m spacing) across a small domain (~50 × 50 m) within Plots A-D. This was done using a GPS snow probe (Snow-Hydro). The reported accuracy of this snow probe was < 0.01 m. The start and end coordinates of each transect were surveyed with a DGPS and used to correct point measurement locations in respective transect. A second 'coarse-grid' set of snow depth measurements covered the entire area in Plots A-D (~160 m × 160 m) with lower sampling density. The coarse-grid snow data were collected using a tile probe, which had an accuracy of approximately 0.01 m. Snow depth was measured every 5 m along five parallel lines in the coarse grid, which were spaced 40 m apart. The total number of data points in each plot was 380.

Ground penetrating radar (GPR) data were acquired over the four study plots and along three transects. The instrument (Mala ProEx with 500 MHz antenna) was pulled on a sled. In each plot, we acquired the GPR data at 0.1-m intervals (marked by an odometer) along 37 lines of 4-m spacing. Several of the GPR lines were co-located with the 'coarse-grid' probe measurements. The GPR technique allowed for denser sampling within the plot relative to the tile probe, with more than 50,000 points in each plot, while the exact location of each measurement was within ~1 m (marked by tape majors). The GPR data were pre-processed to maximize signal-to-noise ratio; a detailed explanation of the use and processing of GPR at this study site was provided by Hubbard et al. (2013). Our pre-processing routine consisted of (1) picking the airwave (which is used to define the signal initiation time, or 'zero time'), (2) picking the travel time of the reflection of the GPR signal that travelled from the snow surface to the snow-ground interface and back to the snow surface, (3) subtracting the zero time from the reflection pick and (4) dividing by two to obtain a one-way travel time between the snow surface and ground surface. A more detailed explanation on the use of GPR in the tundra can be found in Hubbard et al. (2013).

Additional campaigns were carried out in 2014 and 2015 along the transects. UAS and PhoDAR data were collected in July 2013 and 2014 to estimate snow-free ground surface elevation and in May 2015 for estimating snow depth along the transects. To make these measurements, we lifted a consumer-grade digital camera (Sony Nex-5R) to about 40 meters above the ground surface

The Cryosphere Discuss., doi:10.5194/tc-2016-168, 2016
Manuscript under review for journal The Cryosphere
Published: 30 August 2016

using a kite, and acquired downward-looking Red-Green-Blue landscape images, as well as collected some surface elevation data (method described in Smith et al., 2009). The reconstruction procedure was performed using a commercial computer vision software package (PhotoScan from Agisoft LLC). Reconstruction involved automatic image feature detection/matching, structure-from-motion and multiview-stereo techniques for 3D point-cloud generation, and georeferenced mosaic reconstruction. High-accuracy georeferencing was enabled by using a network of ground control points placed on the ground (in summer) and on the snow (in winter) that were surveyed with a high-precision centimeter-grade RTK DGPS system. The snow-free ground surface elevation measurements were then subtracted from the snow surface data to estimate the snow depth over the area. The snow probe measurements were taken at 183 locations to validate the UAS-based snow depth estimates.

The Cryosphere Discuss., doi:10.5194/tc-2016-168, 2016
Manuscript under review for journal The Cryosphere
Published: 30 August 2016

3. Methodology

3.1. GPR Snow Depth Analysis

Snow depth can be inferred by multiplying GPR one-way travel time by radar velocity. The radar velocity is determined by the dielectric constant, which depends on snow density in dry snow (Tiuri, et al., 1984; Harper and Bradford, 2003). Although the snow density is known to be variable in a vertical direction, we assume that the depth-averaged radar velocity—which is a function of depth-averaged snow density—is sufficient in this study for estimating snow depth. Thus, we compute the radar velocity based on the known snow depth from co-located probe measurements as: (radar velocity) = (probe-based snow depth)/(GPR one-way travel time).

Identifying co-located points between the GPR and snow probe measurements, however, is not a trivial task in polygonal ground, since the topography and snow depth can vary significantly within a meter. To address these issues, we investigate the correlations between the radar velocity and the variability of topography. We assume that the effect of positioning errors is larger near the edge of polygons, or in the region where the topographic variability is high. We consider that the uncertainty of radar velocity can be reduced by not using the co-located probe measurements in regions of high topographic variability. To define the topographic variability, we compute the elevation difference within a 1-meter radius of each probe measurement. In addition, the reflections from the troughs could originate from the edge of polygons rather than the location right below the GPR instrument. Such an "edge reflection" effect can lead to underestimation of the radar velocity. We assume that we could detect the presence of the edge reflection by evaluating the systematic bias (i.e., underestimation) in the radar velocity in relation to the topographic variability.

The Cryosphere Discuss., doi:10.5194/tc-2016-168, 2016
Manuscript under review for journal The Cryosphere
Published: 30 August 2016

3.2. UAS Snow Depth Analysis

We first evaluate the accuracy of the UAS-derived digital surface model (DSM) by comparing it to the GPS elevation measurements along the transects. Since the UAS-derived DSM was obtained at very high lateral resolution (4 cm by 4 cm), it was more prone to noise or small scale variability (Nolan et al., 2015). As such, we test three schemes to explore the co-location between the two datasets: (1) nearest points, (2) average elevation within the 0.5-m radius, and (3) minimum elevation within the 0.5-m radius. We then compare the snow depth estimate from UAS and probe measurements at co-located points. In the same manner as the GPR data, we eliminate the probe measurements in the regions where the topographic variability is high.

3.3. Spatial Variability Analysis of Topography and Snow Depth

To quantify the topographic effects in a complex terrain of ice-wedge polygons and to partition micro- and macrotopography, we apply the wavelet transform method to the airborne LiDAR DEM, which is commonly used for 2D image processing. The wavelet approach has recently been applied to DEM for geomorphic studies, including terrain analysis and landslide analysis (Bjørke and Nilsen, 2003; Kalbermatten, 2010; Kalbermatten et al., 2012). In this transform, a high-pass filter (a mother wavelet) and a low-pass filter (a father wavelet) are applied to decompose the DEM into four images at each scale: low-pass, high-pass horizontal, high-pass vertical, and high-pass diagonal images). Depending on the scale of the wavelet transform, the method yields different images, corresponding to different scales of topographic features. We define this wavelet scale as a *topography separation scale*. We consider the low-pass image as *macrotopographic elevation* (i.e., the smoothed version of the original DEM) and the high-pass image as *microtopographic elevation* (i.e., the topographic variability associated with ice-wedge polygon development).

Correlations between the topographic metrics and snow depth are identified using the Pearson product-moment correlation coefficient (Anderson et al., 2014). At each spatial scale, we can compute micro- and macrotopographic metrics such as slope and curvature as well as their correlations with corresponding probe-measured snow depth. The curvature is of particular interest, since Dvornikov et al. (2015) reported strong correlations between snow surface curvature and snow depth, and a dependency of this correlation on the DEM resolution. Note that the DEM resolution (0.5 m) in this study is much finer than the one (25 m) in Dvornikov et al. (2015). We compute a wind factor in a similar manner as Dvornikov et al. (2015), with a slight modification. Here we define the wind factor as the inner product of the slope direction and predominant wind direction. With this calculation, the wind factor is smallest in the slope against the wind direction, and largest in the slope in line with the wind, which is reasonable and also consistent with visual observations at the site. When the correlation is statistically significant, the metrics are included in a regression analysis (Davison, 2003) to represent the snow depth as a function of the topographic metrics.

A geostatistical approach has been used to investigate the spatial variability of snow depth as well as the scales of variability (Anderson et al., 2014). The standard geostatistical analysis starts with creating an empirical variogram, followed by estimating the spatial correlation parameters (Diggle and Ribeiro, 2007). The spatial correlation parameters include (1) magnitude of variability (or spatial heterogeneity) as variance, (2) fraction of correlated and uncorrelated variability (nugget ratio), (3) spatial correlation length (range), and (4) covariance model (i.e., the shape of decay in the spatial correlation as a function of distance), such as exponential and spherical models. Such spatial variability and correlation are particularly important for interpolating the sparse snow depth measurements. The interpolation can be applied not only for snow depth itself but also for snow surface (snow depth plus elevation) or residual snow depth after removing topographic correlations in the regression analysis. The same geostatistical analysis are therefore performed for snow surface and residual snow depth.

3.4. Bayesian Geostatistical Estimation Method

We first define that the snow depth at each pixel y_i ($i = 1,\ldots, n$) is a hidden variable which can be observed only with an added measurement error. In this study, we set the pixel size to 0.5 by 0.5 m, which corresponded to the LiDAR DEM resolution. The snow depth distribution (or field) is defined by a vector $\boldsymbol{y} = \{y_i|\ i = 1, \ldots, n\}$. We integrate three datasets: point-probe data $\boldsymbol{z}_\mathrm{p}$, GPR data $\boldsymbol{z}_\mathrm{g}$, and LiDAR DEM $\boldsymbol{z}_\mathrm{d}$. The goal of the estimation is to determine the posterior distribution of snow depth conditioned on all the given datasets, $p(\boldsymbol{y}\ |\boldsymbol{z}_\mathrm{p}, \boldsymbol{z}_\mathrm{g}, \boldsymbol{z}_\mathrm{d})$. Following a Bayesian hierarchical approach, we divide this posterior distribution into three sets of statistical sub-models (Wikle et al., 2001; Wainwright et al., 2014; 2016). First, *data models* represent each data value as a function of snow depth at each pixel, depending on different data types. Second, *process models* describe the spatial distribution of snow depth (i.e., snow depth field) as function of topography and correlation parameters. Finally, *prior models* define the prior information of parameters. The hierarchical approach breaks down a complex posterior distribution into a series of simple models, and hence enables us to capture complex relationships easily. In addition to the snow field vector and data vectors, two parameter vectors are defined: the process-model parameter vector $\boldsymbol{a}$ to represent the heterogeneous pattern of snow depth, and the data-model parameter vector $\boldsymbol{b}$ to describe the correlations between the snow depth and the GPR travel time.

We assume a linear model to describe the snow depth field,

$$\boldsymbol{y} = \mathbf{A}\boldsymbol{a} + \boldsymbol{\tau} \tag{1}$$

where A is the design matrix as a function of the topographic metrics as explanatory variables (and hence a function of DEM z_d). The process-model parameter vector $\boldsymbol{a}$ describes the correlation between the topographic metrics and the snow depth field. We assume that the residual of this correlation $\boldsymbol{\tau}$ represents the unexplained variability by the topographic metrics and that $\boldsymbol{\tau}$ is spatially correlated. The residual term $\boldsymbol{\tau}$ is described by a multivariate normal distribution with a covariance Σ, which is determined by a geostatistical analysis (Diggle and Ribeiro, 2007).

The data model for the probe measurements defines the probe data z_p as a function of snow depth $\boldsymbol{y}$:

$$\boldsymbol{z}_p = \boldsymbol{y} + \boldsymbol{\varepsilon}_p \tag{2}$$

We assume that the vector $\boldsymbol{\varepsilon}_p$ is an uncorrelated normally-distributed measurement error at each data location with the standard deviation of σ_p. We determine the error based on the accuracy estimate of each probe. The probe data vector z_p follows a multivariate normal distribution with the mean vector $\boldsymbol{y}$ and the covariance matrix D_p, which is a diagonal matrix with with diagonal elements of σ_p^2.

The Cryosphere Discuss., doi:10.5194/tc-2016-168, 2016
Manuscript under review for journal The Cryosphere
Published: 30 August 2016

The data model for the GPR data describes the GPR data z_g as a function of the snow depth $\boldsymbol{y}$ at the GPR locations. The GPR data model can be represented by a linear model:

$$\boldsymbol{z}_g = b_0 + \mathrm{B}\boldsymbol{y} + \boldsymbol{\varepsilon}_g \tag{3}$$

where B is a matrix, the diagonal elements of which is b_1. The error vector ε_g is an uncorrelated normally-distributed measurement error with the standard deviation of σ_g. The standard deviation is computed from comparing the GPR-based snow depth to the probe-based one. At the same time, the GPR data model can be written as a function of the parameter vector $\boldsymbol{b}$ such that:

$$\boldsymbol{z}_g = \mathrm{Y}\boldsymbol{b} + \boldsymbol{\varepsilon}_g \tag{4}$$

where Y is the design matrix with the first column being $\boldsymbol{y}$, and the second column being all one. The parameter vector $\boldsymbol{b} = \{b_1, b_0\}$ represents the linear correlations between the GPR data and snow depth. This alternative model is useful during the estimation procedure described below. The GPR data vector z_g follows a multivariate normal distribution with the mean vector $\boldsymbol{y}$ and the covariance matrix D_g that is a diagonal matrix with with diagonal elements of σ_g^2.

The posterior distribution of the snow depth conditioned on the datasets $p(\boldsymbol{y} \mid z_d, z_p, z_g)$ is a marginal distribution of $p(\boldsymbol{y}, \boldsymbol{a}, \boldsymbol{b} \mid z_d, z_p, z_g)$. By applying Bayes's rule and following the conditional dependencies defined above, we can decompose this posterior distribution as:

$$p(\boldsymbol{y}, \boldsymbol{a}, \boldsymbol{b} \mid z_d, z_p, z_g) \propto p(z_g \mid \boldsymbol{y}, \boldsymbol{b})\, p(z_p \mid \boldsymbol{y})\, p(\boldsymbol{y} \mid \boldsymbol{a}, z_d) p(\boldsymbol{a}) p(\boldsymbol{b}). \tag{5}$$

Table 1 defines all the distributions on the right-hand side of Equation (5) based on the models defined in Equations (1) – (4). We also assume multivariate normal distributions for the prior distributions of the parameter vectors $\boldsymbol{a}$ and $\boldsymbol{b}$. The posterior distribution in Equation (5) can be computed using the Markov-chain Monte-Carlo method (Gamerman and Lopes, 2006). Since all the distributions are defined as multivariate normal distributions, it is possible to use efficient

The Cryosphere Discuss., doi:10.5194/tc-2016-168, 2016
Manuscript under review for journal The Cryosphere
Published: 30 August 2016

Gibbs' algorithm. The MCMC procedure is described in Appendix A. The convergence can be confirmed by the Geweke's convergence diagnostic (Geweke, 1992).

The Cryosphere Discuss., doi:10.5194/tc-2016-168, 2016
Manuscript under review for journal The Cryosphere
Published: 30 August 2016

4. Results

4.1. Snow Depth Measurements

GPR Radar Velocity Analysis

Our results indicate that the estimated radar velocity does not have a systematic dependency on (or trend with) the snow depth or topographic variability (Figures 2a and 2b). The variability of the radar velocity, on the other hand, depends on those two factors (i.e., the variability of snow depth and the one of topography). The variability is higher at shallower snow depth (Figure 2a), and also in localized regions of large topographic variability (Figure 2b). By selecting the points with a topographic variability < 0.05 m, we obtained a mean radar velocity of 0.25 m/ns, which was used for subsequent analysis.

Using the mean velocity value, the calculated GPR-based snow depth estimates were compared with the probe measurements (Figure 2c). The correlation between the measured and estimated is high, with the root mean square error (RMSE) being 5.4 cm, and with no significant under- or overestimation (the mean bias error –0.16 cm). The selected points in the regions of low topographic variability (red circles) are more tightly distributed around the one-to-one line. In these regions, the RMSE of GPR-based snow depth improved to 2.9 cm.

Snow Depth Measurements in Different Polygon Types

Figure 3 shows the LiDAR DEM as well as snow probe measurements and GPR estimates in Plots A–D. The LiDAR DEM (in the left column) illustrates the difference among four plots in terms of both macro- and microtopography. For example, Plot A has better defined polygon rims and troughs than Plot D, although Plot A and D are both low-centered polygons. Plot B has

The Cryosphere Discuss., doi:10.5194/tc-2016-168, 2016
Manuscript under review for journal The Cryosphere
Published: 30 August 2016

round-shaped high-centered polygons, while Plot C has flat-centered polygons with well-defined troughs. The average size of polygons is also different, with smaller polygons in Plot B and larger polygons in Plots A, C and D. In addition, these figures illustrate some macrotopographic trends. Plot C is gradually sloping down towards the east, and Plot D has a depression (i.e., DTLB) in the northeastern half.

The middle column in Figure 3 shows the snow probe data collected using the fine-grid and coarse-grid scheme. The fine-grid data reveals the detailed heterogeneity of snow depth around a single polygon. For example, the fine-grid data in Plot A show the snow depth distribution in a low-centered polygon, including thin snow along the polygon rim and thick snow at the polygon center and trough. Comparison of the fine-grid snow data with the DEM reveals that they are mirror images of each other. The coarse-grid dataset covers the entire plot, although it is much more difficult to ascertain the relationship between the snow depth and microtopography. The probe data show that the snow depth is highly variable, ranging from 0.2 m to 0.8 m in a single plot.

In the third column of Figure 3, the snow depth was estimated from GPR using a fixed radar velocity 0.25 m/ns along the lines, and then interpolated with a simple linear interpolation in between the lines. The GPR estimates clearly reveal the influence of microtopography on snow depth at the resolution of a single-polygon scale and over the entire plot. The high-resolution snow estimates over the large area allow us to visually identify the macrotopographic control on snow depth. In Plot C, for example, the snow depth does not have an increasing or decreasing trend, even though the elevation gradually decreases towards east. Plot D, on the other hand, has more snow accumulation in the eastern part of the domain, which is in the depression associated with DTLB.

UAS-based Snow Depth Measurements

In the region of the transects, the UAS-derived snow-free DSM (Figure 4a) was first compared with the GPS data in Table 2, using the different schemes to identify co-location. Taking the average in the vicinity of each probe measurement provides the lowest RMSE (RMSE = 6.0 cm), which is approximately the same as the LiDAR data (RMSE = 6.08 cm). The UAS-derived snow depth estimates were obtained by differencing the snow surface and snow-free DSM (Figure 4b). The comparison between the UAS-based snow estimates and the probe data are favorable (Figure 4c), with a RMSE of 6.0 cm. When we removed the points that had a large topographic variability in the vicinity (in the same way as the GPR snow depth analysis), the RMSE improved to 4.6 cm (Figure 4c)

The UAS-derived snow depth (Figure 4b) reveals a similar pattern of snow distribution as the GPR data in Figure 3, having deeper snow in the troughs and the centers of low-centered polygons. The high-resolution image of the UAS data reveals more detail of the microtopographic effect than the interpolated image of the GPR data in Figure 3, particularly in the narrow troughs. The large aerial coverage also shows the effect of macrotopography: while the elevation decreases towards south, the snow depth does not have a large-scale trend.

4.2. Snow Depth Variability over Tundra

Variability among Different Polygon Types

The Cryosphere Discuss., doi:10.5194/tc-2016-168, 2016
Manuscript under review for journal The Cryosphere
Published: 30 August 2016

Figure 5 shows the boxplots of the snow depth, elevation, and microtopographic elevation (Δelevation) in each plot. We used the coarse-grid probe measurements, since the samples are uniformly distributed over each plot. The median snow depth (Figure 5a) is fairly similar among four plots, even though they have different geomorphologic features and polygon types. Tukey's pairwise comparison test (Table 3) shows that only Plot B (small high-centered polygons) is significantly different from the other plots.

The absolute elevation distribution varies among the four plots (Figure 5b), although the snow depth for each of the plots has similar median values and distributions. Plot A (well-defined low-centered polygons), for example, is at a higher elevation than Plots C (flat-centered polygons) and D (low-centered polygons in DTLB), but the difference in the average snow depth is not statistically significant (Table 3). The microtopographic elevation is computed based on the wavelet transform with the scale of 32 m, removing the difference in the macrotopographic elevation among the four plots (Figure 5b). Plot D (low-centered polygons in DTLB), for example, has less variability in both elevation and snow depth, because Plot D has less distinct microtopography than others. In contrast, Plot B has large variability in both microtopography and snow depth.

Correlations between Snow Depth and Topographic Indices

Among the topographic indices of macro- and microtopography, the snow depth was significantly correlated only to the microtopographic elevation for all plots (Figure 6a). The correlation coefficient changes with the scale of the wavelet transform that separates micro- and macrotopography. The correlation coefficient is up to –0.8 at Plot B (small high-centered polygons), and up to –0.7 at all the data points. The correlation coefficient is different among different plots (i.e., different polygon types); the correlation is less significant at Plot D (low-centered polygons in DTLB), than other plots. The best correlation (i.e., the largest absolute value) can be achieved at a different scale in each plot (Plot B < Plot A and Plot C < Plot D).

A significant correlation between snow depth and wind factor of macrotopography was identified only in Plot D (low-centered polygons in DTLB; Figure 6b). The correlation coefficient is up to 0.41 at the scale of 38 m. Other topographic indices (i.e., the slope and curvature of both micro- and macrotopography, the wind factor of microtopography) are not shown here, since we did not find any significant correlation. Although Dvornikov et al. (2015) reported a strong correlation between snow depth and curvature (snow free DEM), we did not find any significant correlation in our data.

Geostatistical Analysis of Snow Depth

Spatial correlation exists for all three variables: snow depth, snow surface, and residual snow depth after removing the correlation to the microtopographic elevation (Table 4). The correlation range is less than 20 m for the snow depth, which is consistent with the large variability in a short distance. The snow surface, on the other hand, has a larger correlation range (253 m). Such a large correlation length is consistent with the field observation that the snow surface is smooth across the site. The variance is comparable between the snow depth and snow surface, while the variance is much lower in the residual snow depth, since the topographic correlation explains a large portion of the snow depth variability.

The Cryosphere Discuss., doi:10.5194/tc-2016-168, 2016
Manuscript under review for journal The Cryosphere
Published: 30 August 2016

4.3. Snow Depth Estimation based on LiDAR DEM

Based on the snow-topography analysis in Section 4.2, we included the linear correlation between snow and microtopographic elevation in Equation (1) to describe the snow variability. The first column of the design matrix A is the microtopographic elevation at all the pixels, and the second one is a vector of all ones. The parameter vector ***a*** is a 2-by-1 vector with the linear correlation parameters (slope and intercept). The Bayesian method (Section 3.4) yielded 10,000 equally likely fields of the snow depth from the posterior distribution in Equation (5).

The estimated mean snow-depth field over the entire study region (Figure 7a) captures the effects of microtopography, such as more snow accumulation in polygon troughs and centers of low-centered polygons. The snow depth does not have a large-scale trend over the domain, which is different from the LiDAR DEM in Figure 1, but consistent with the ground-based measurements (Figure 3 and 4). The variability is larger in the southern region where there are high-centered polygons with deep troughs. In addition, we compared this result with the mean field based on the kriging-based interpolation of the snow surface elevation (Diggle and Ribeiro, 2007) and subtracting the ground surface elevation (Figure 7b). The two mean fields are similar, particularly in the central regions that have many measurements.

The estimated standard deviation of snow depth over the region (Figure 8a), on the other hand, shows a significant difference from the one based on the snow surface interpolation (Figure 8b). This standard deviation represents the uncertainty in the estimation. In both cases, the standard deviation is smaller near the measurement locations along the transects and within the four plots. However, when the topographic correlation is included (Figure 8a), the standard deviation

The Cryosphere Discuss., doi:10.5194/tc-2016-168, 2016
Manuscript under review for journal The Cryosphere
Published: 30 August 2016

increases more rapidly as the pixel is farther away from the data points. This is due to the fact that the spatial correlation range is small for the residual snow depth after removing the topographic correlation (Table 4).

Validation of the snow depth estimates over the study area was performed by comparing the estimates with the probe data not used in the procedure (randomly selected). The validation results (Figure 9) show that the estimated confidence interval captures the probe-measured snow depth. The estimated snow depth is distributed along with the one-to-one line without any significant bias. The estimation, including the topographic correlation (Figure 9a), has a tighter confidence interval and better estimation results than the one from interpolating the snow surface (Figure 9b). The RMSE for including the topographic correlations is 6.0 cm, while the one for interpolating the snow surface is 8.8 cm.

5. Discussion

5.1. Different Observational Platforms

Our analysis showed that GPR data provided the end-of-winter snow depth distribution with high accuracy (RMSE = 2.9 cm) and resolution (10 cm along each line). The GPR-based estimation requires care, particularly regarding the estimation of radar velocity and associated possible errors, such as those due to positioning. Although the radar velocity is known to depend on the snow density, we attribute the variability of radar velocity at our site to random or positioning errors. Three results support this claim. First, the variability is smaller in a thicker snow pack, suggesting the small contribution of the error relative to the overall snow depth. Second, the radar velocity variability depends on the variability of the topography in the vicinity of the calibration points, suggesting the impact of positioning errors. Third, there was no systematic trend in the radar velocity as a function of the snow depth or topographic positions. We developed a simple methodology to select co-located calibration points based on the variability of topography, which proved to be useful to compute accurate velocity. We note that the snow density could be variable vertically along the depth; we indeed found some layers of ice created by winter rain events in the middle of the snow pack. It is possible that there might be a difference in the depth-averaged density and radar velocity at a later time, when the snow pack starts to melt in a heterogeneous manner.

UAS-based PhoDAR provided an attractive alternative for estimating snow depth at high resolution over a large area. With much less labor and time, UAS can provide many more sample points than GPR. The UAS-based snow depth, however, was less accurate than ground-based GPR or point probe measurements (RMSE = 6.0 cm). The main contribution of this error resulted from the snow-free elevation, since RMSE for the surface DSM is around 6 cm. We note that the RMSE of 6.0 cm is still significantly more accurate than the previous LiDAR and other airborne surveys (e.g., Deems et al., 2013; Harpold et al. 2014; Nolan et al., 2015).

The UAS-based approach is expected to continue its trajectory of continuous improvements in terms of technical aspects, ease of use, and accuracy. At the time of our campaign, we were allowed to use only a kite due to regulations, which led to a limited number of pictures that could be used to reconstruct the DSM. The accuracy will significantly improve with the use of a light unmanned aerial vehicle (UAV). Although UAS-based LiDAR acquisition technology continues to improve (e.g., Anderson and Gaston, 2013), and is expected to be a powerful alternative to characterize snow, the LiDAR device is still significantly more expensive than a conventional camera (roughly by factor of 100). Given that the vegetation height is fairly small in the Arctic tundra, the PhoDAR technique is an affordable option.

5.2. Snow Depth Variability

The end-of-year snow depth distribution at the ice-wedge polygons was highly variable over a short distance. The snow depth was, however, significantly correlated with the microtopographic elevation, suggesting that the snow depth could be described by microtopography. The wind-blown snow transport leads to significant snow redistribution, and fills microtopographic lows (i.e., troughs and centers of low-centered polygons) with thicker snow pack (e.g., Pomeroy et al., 1993). The redistribution also results in the smooth snow surface, following the macrotopography. The exception was observed at the edge of the DTLB, where the abrupt change in macrotopography led to increased accumulation in the depression. This is a similar effect to that observed along the riverbanks by Benson and Sturm (1993). Although the tundra ecosystem studies have focused on the effect of microtopography (e.g., Zona et al., 2011), the macrotopography also may be important when we characterize snow distribution over a larger area.

The "average" snow depth over a hundred-meter scale, on the other hand, was fairly uniform across the site despite the different polygon types. Plot A (well-defined low-centered polygons) and C (flat-centered polygons), for example, have different polygon types, but they have a similar average snow depth. This is because microtopography and microtopographic features (i.e., polygon troughs, rims) mainly control the snow distribution. Plot B (small high-centered polygons) is an exception, having smaller median snow depth than the other plots. Plot B has the largest variability in microtopography, characterized by the small round high-centered polygons, like numerous small mounds (Figure 3). Such mounds are prone to erosion by the wind, and hence lead to less snow trapping and accumulation.

Identifying such correlations between snow depth and topography requires an effective approach to separate micro- and macrotopography. Our wavelet analysis revealed that the separation scale depends on the polygon sizes; for example, the larger polygons in Plot A (well-defined low-centered polygons) and C (flat-centered polygons) lead to a larger separation scale than the smaller polygons in Plot B (small high-centered polygons). It is a challenge to map macrotopography accurately over a larger area, particularly at the present site, where different types and sizes of polygons mix. Although we used the same scale for the estimation, the improved polygon delineation algorithm will possibly enable us to separate micro- and macrotopography in the future (e.g., Wainwright et al., 2015).

5.3. Snow Depth Estimation

The developed Bayesian approach enabled us to estimate the snow depth distribution over a large area based on the LiDAR DEM and the correlation between the snow depth and topography. Although this paper only used the ground-based GPR and probe measurements collected at the same time, UAS could be easily included in the same framework. The Bayesian method allowed us to integrate three types datasets (LiDAR DEM, probe and GPR) in a consistent manner, and also provided the uncertainty estimate for the estimated snow depth. Taking into account the topographic correlation explicitly improved the accuracy of estimation significantly, compared to interpolating the snow surface and subtracting the DEM.

Our approach can be extended to snow estimates over both time and space. The correlations between snow depth and topography may change over time. In early and later winter, for example, the snow depth would be more affected by curvature and slope of microtopography, since the microtopographic lows (troughs and centers of the low-centered polygons) are not filled by snow. It would be possible to quantify the changes in the topography-snow correlations by designing ground-based measurements and remote sensing snow surface measurements (by UAS). The Bayesian method presented here is flexible enough to account for changes in parameters over time for the spatial-temporal data integration (e.g., Wikle et al., 2001). Although physically-based snow distribution models can be used for the same purposes (e.g., Pomeroy et al., 1993; Liston and Sturm, 1998; 2002), it is difficult to parameterize all the processes, such as

The Cryosphere Discuss., doi:10.5194/tc-2016-168, 2016
Manuscript under review for journal The Cryosphere
Published: 30 August 2016

sublimation and turbulent transport. Our data-driven approach provides a powerful alternative to distribute snow depth based on various datasets.

The Cryosphere Discuss., doi:10.5194/tc-2016-168, 2016
Manuscript under review for journal The Cryosphere
Published: 30 August 2016

6. Summary

In this study, we explored various strategies to estimate the end-of-year snow depth distribution over an Arctic ice wedge polygon tundra region. We first developed an effective methodology to calibrate GPR and UAS in the presence of complex microtopographic variability. We then investigated the characteristics and accuracy of three observational platforms: point probe, GPR and UAS. Although UAS showed a great potential for characterizing the snow depth over a large area, the ground-based observations were still more accurate.

We investigated the spatial variability of the snow depth and its dependency on the topographic metrics. At the peak snow depth during our data acquisition, the snow depth was highly correlated with microtopographic elevation, although it was highly variable over short distances. The wind redistribution created a smooth snow surface, following macrotopography at the site. The challenge was to separate macro- and microtopography, since the separation scale was not arbitrary, and depended on the polygon size. The wavelet analysis provided an effective approach to identify this separation scale.

The Bayesian method was effective at integrating different measurements to estimate snow depth distribution over the site. Although our estimation is based on the data collected from a one-time campaign, and the correlations to topography may change over time, the approach developed here is expected to be extensible for estimating both spatial and temporal variability of snow depth and for exploring the influence of snow depth on ecosystem functioning.

The Cryosphere Discuss., doi:10.5194/tc-2016-168, 2016
Manuscript under review for journal The Cryosphere
Published: 30 August 2016

Appendix A

In MCMC, we sample each variable sequentially conditioned on all the other variables. In other words, when we update one variable (or one vector), we assume that the other variables are known and fixed. After sampling thousands of sets of the variables, the distribution of those samples converges to the posterior distribution. Each vector is sampled as follows:

The snow depth field is sampled from the distribution:

$$p(\boldsymbol{y} \mid \bullet) = p(\boldsymbol{y} \mid \boldsymbol{a}, \boldsymbol{b}, z_{\mathrm{d}}, z_{\mathrm{g}}, z_{\mathrm{p}}) \propto p(z_{\mathrm{g}} \mid \boldsymbol{y}, \boldsymbol{b})\, p(z_{\mathrm{p}} \mid \boldsymbol{y})\, p(\boldsymbol{y} \mid \boldsymbol{a}, z_{\mathrm{d}}) \tag{A.1}$$

where "•" represents all the other variables. The distribution is decomposed to a series of small conditional distributions defined in Table 1. Similarly, we can sample the snow-process parameters $\boldsymbol{a}$ and GPR-data parameter $\boldsymbol{b}$ from the distributions:

$$p(\boldsymbol{a} \mid \bullet) = p(\boldsymbol{a} \mid \boldsymbol{y}, \boldsymbol{h}) \propto p(\boldsymbol{y} \mid \boldsymbol{h}, \boldsymbol{a})\, p(\boldsymbol{a}) \tag{A.2}$$

$$p(\boldsymbol{b} \mid \bullet) = p(\boldsymbol{b} \mid \boldsymbol{y}, z_{\mathrm{g}}) \propto p(z_{\mathrm{g}} \mid \boldsymbol{y}, \boldsymbol{b})\, p(\boldsymbol{b}) \tag{A.3}$$

Since all the distributions in Equation A.1–A.3 are multivariate Gaussian, we can use the conjugate prior to compute an analytical form of each distribution. Each distribution is multivariate Gaussian with the covariance and mean vector defined in Table A.1. In the Gibbs' sampling algorithm, we sample each variable vector sequentially until the distributions are converged.

Acknowledgements

The Next-Generation Ecosystem Experiments (NGEE Arctic) project is supported by the Office of Biological and Environmental Research in the DOE Office of Science. This NGEE-Arctic research is supported through contract number DE-AC0205CH11231 to Lawrence Berkeley National Laboratory. We gratefully acknowledge Stan Wullschleger in Oak Ridge National Laboratory, project PI. We thank Dr. Craig Tweedie at University of Texas, El Paso for providing the LiDAR dataset, and together with Sergio Vargas from University of Texas, El Paso, for providing kite-based landscape imaging advice. Datasets are available upon request by contacting the corresponding author (Haruko M. Wainwright, hmwainwright@lbl.gov).

The Cryosphere Discuss., doi:10.5194/tc-2016-168, 2016
Manuscript under review for journal The Cryosphere
Published: 30 August 2016

Reference:

Anderson, B. T., McNamara, J. P., Marshall, H. P., & Flores, A. N. (2014). Insights into the physical processes controlling correlations between snow distribution and terrain properties. Water Resources Research, 50(6), 4545-4563.

Anderson, K., and Gaston, K. J. (2013). Lightweight unmanned aerial vehicles will revolutionize spatial ecology. Frontiers in Ecology and the Environment, 11(3), 138-146.

Benson, C. S., and Sturm, M. (1993). Structure and wind transport of seasonal snow on the Arctic slope of Alaska. Annals of Glaciology, 18, 261-267.

Binley, A., Hubbard, S.S., Huisman, J., Revil, A., Robinson, D., Singha, K., and Slater, L. (2015) The emergence of hydrogeophysics for improved understanding of subsurface processes over multiple scales. DOI: 10.1002/20015WR017016

Bowling, L. C., D. L. Kane, R. E. Gieck, L. D. Hinzman, and D. P. Lettenmaier, The role of surface storage in a low-gradient Arctic watershed, Water Resour. Res., 39(4), 1087, doi:10.1029/2002WR001466, 2003.

Bjørke, J. T., and Nilsen, S. (2003). Wavelets applied to simplification of digital terrain models. International Journal of Geographical Information Science, 17(7), 601-621.

Brown, J. (1967), Tundra soils formed over ice wedges, northern Alaska, Soil Sci. Soc. Am. J., 31(5), 686–691

Callaghan, T. V., M. Johansson, R.D. Brown, P. Y. Groisman, N. Labba, V. Radionov, R.S. Bradley, S. Blangy, O.N. Bulygina, T.R. Christensen, J.E. Colman, R.L.H. Essery, B.C. Forbes, M.C. Forchhammer, V.N. Golubev, R. E. Honrath, G.P. Juday, A.V. Meshcherskaya, G.K. Phoenix, J. Pomeroy, A. Rautio, D.A. Robinson, N.M. Schmidt, M.C. Serreze, V.P. Shevchenko, A.I. Shiklomanov, A.B. Shmakin, P. Sköld, M. Sturm, M. Woo, E. F. Wood,

The Cryosphere Discuss., doi:10.5194/tc-2016-168, 2016
Manuscript under review for journal The Cryosphere
Published: 30 August 2016

(2011). Multiple Effects of Changes in Arctic Snow Cover. Ambio, 40 (Suppl 1), 32–45. doi:10.1007/s13280-011-0213-x

Clein, J. S., & Schimel, J. P. (1995). Microbial activity of tundra and taiga soils at sub-zero temperatures. Soil Biology and Biochemistry, 27(9), 1231-1234.

Davison, A. C. (2003). Statistical models (Vol. 11). Cambridge University Press.

Deems, J. S., Painter, T. H., & Finnegan, D. C. (2013). Lidar measurement of snow depth: a review. Journal of Glaciology, 59(215), 467-479.

Diggle, P. and Ribeiro, P. J. (2007). Model-based geostatistics. Springer Science & Business Media.

Dvornikov, Y., Khomutov, Mullanurov, and Ermokhina (2015), GIS- and field data based modeling of snow water equivalent in shrub tundra, Ice and Snow, doi:10.15356/2076-6734-2015-2-69-80.

Gamerman, D. and H. F. Lopes (2006), Markov Chain Monte Carlo - Stochastic simulation for Bayesian inference. Chapman&Hall/CRC, 2nd edition, Boca Raton, USA.

Gamon, J. A., G. P. Kershaw, S. Williamson, and D. S. Hik (2012), Microtopographic patterns in an arctic baydjarakh field: do fine-grain patterns enforce landscape stability? Environ. Res. Lett., 7(1), 015502.

Geweke, J. (1992), Evaluating the accuracy of sampling-based approaches to calculating posterior moments, in Bayesian Statistics 4 (edited by J. M. Bernado, J. O. Berger, A. P. Dawid and A. F. M. Smith), Clarendon Press, Oxford, UK.

Gusmeroli, A., and Grosse, G. (2012). Ground penetrating radar detection of subsnow slush on ice-covered lakes in interior Alaska. The Cryosphere, 6(6), 1435-1443.

The Cryosphere Discuss., doi:10.5194/tc-2016-168, 2016
Manuscript under review for journal The Cryosphere
Published: 30 August 2016

Gusmeroli, A., G. Wolken, and A. Arendt (2014), Helicopter-borne radar imaging of snow cover on and around glaciers in Alaska, Annals of Glaciology, 55(67), 78–88, doi:10.3189/2014aog67a029.

Harper, JT, and JH Bradford (2003), Snow stratigraphy over a uniform depositional surface: spatial variability and measurement tools, Cold Regions Science and Technology.

Harpold, A. A., et al. (2014), LiDAR-derived snowpack data sets from mixed conifer forests across the Western United States, Water Resour. Res., 50, doi:10.1002/2013WR013935.

Hinkel, K. M., W. R. Eisner, J. G. Bockheim, F. E. Nelson, K. M. Peterson, and X. Dai (2003), Spatial extent, age, and carbon stocks in drained thaw lake basins on the Barrow Peninsula, Alaska, *Arct., Antarct., and Alp. Res.*, 35(3), 291-300.

Hubbard, S. and Y. Rubin (2005), Hydrogeophysics, Chapter 1 in Hydrogeophysics, Eds. Y. Rubin and S. Hubbard, Elsevier.

Hubbard, S. S., C. Gangodagamage, B. Dafflon, H. Wainwright, J. E. Peterson, A. Gusmeroli, C. Ulrich, Y. Wu, C. Wilson, C., J. Rowland, C. Tweedie, and S. D. Wullschleger (2013), Quantifying and relating land-surface and subsurface variability in permafrost environments using LiDAR and surface geophysical datasets, Hydrogeol. J., 21(1), 149-169.

Jansson, JK, and N Taş (2014), The microbial ecology of permafrost, Nature Reviews Microbiology, doi:10.1038/nrmicro3262.

Kane, D. L., L. D. Hinzman, C. S. Benson, and G. E. Liston (1991), Snow hydrology of a headwater Arctic basin: 1. Physical measurements and process studies, Water Resour. Res., 27(6), 1099–1109, doi:10.1029/91WR00262.

Kalbermatten, M. (2010). Multiscale analysis of high resolution digital elevation models using the wavelet transform, Thesis, Ecole Polytechnique Federale de Lausanne.

The Cryosphere Discuss., doi:10.5194/tc-2016-168, 2016
Manuscript under review for journal The Cryosphere
Published: 30 August 2016

Kalbermatten, M., Van De Ville, D., Turberg, P., Tuia, D., & Joost, S. (2012). Multiscale analysis of geomorphological and geological features in high resolution digital elevation models using the wavelet transform. Geomorphology, 138(1), 352-363.

Liljedahl, A. K., Hinzman, L. D., Harazono, Y., Zona, D., Tweedie, C. E., Hollister, R. D., Engstrom, R., and Oechel, W. C. (2011) Nonlinear controls on evapotranspiration in arctic coastal wetlands, Biogeosciences, 8, 3375-3389, doi:10.5194/bg-8-3375-2011.

Liljedahl, A. K., Boike, J., Daanen, R. P., Fedorov, A. N., Frost, G. V., Grosse, G., ... & Necsoiu, M. (2016). Pan-Arctic ice-wedge degradation in warming permafrost and its influence on tundra hydrology. Nature Geoscience.

Liston, G. E., and Sturm, M. (1998). A snow-transport model for complex terrain. Journal of Glaciology, 44(148), 498-516.

Liston, G., and Sturm, M. (2002). Winter precipitation patterns in arctic Alaska determined from a blowing-snow model and snow-depth observations. Journal of Hydrometeorology, 3, 646–659.

MacKay, J. R. (2000), Thermally induced movements in ice-wedge polygons, western Arctic coast: a long-term study, *Géographie physique et Quaternaire*, 54(1), 41-68.

Machguth, H, O. Eisen, F. Paul, and M Hoelzle (2006), Strong spatial variability of snow accumulation observed with helicopter borne GPR on two adjacent Alpine glaciers, Geophysical Research Letters, 33(13), doi:10.1029/2006GL026576.

Nobrega, S, and P Grogan (2007), Deeper snow enhances winter respiration from both plant-associated and bulk soil carbon pools in birch hummock tundra, Ecosystems, doi:10.1007/s10021-007-9033-z.

The Cryosphere Discuss., doi:10.5194/tc-2016-168, 2016
Manuscript under review for journal The Cryosphere
Published: 30 August 2016

Nolan, M., C. Larsen, and M. Sturm (2015), Mapping snow depth from manned aircraft on landscape scales at centimeter resolution using structure-from-motion photogrammetry, Cryosphere, 9(4), 1445–1463, doi:10.5194/tc-9-1445-2015.

Osterkamp, T. E. (2007), Causes of warming and thawing permafrost in Alaska, Eos Trans. AGU, 88(48), 522–523, doi:10.1029/2007EO480002.

Pomeroy, J.W., Gray, D.M. and Landine, P.G., 1993. The Prairie Blowing Snow Model: characteristics, validation, operation. J. Hydrol., 144: 165-192.

Smith, M.J., J. Chandler, and J. Rose (2009), High spatial resolution data acquisition for the geosciences: kite aerial photography, *Earth Surf. Proc. and Land.*, 34(1), 155-161.

Stieglitz, M., S.J.De ´ry, V. E. Romanovsky, and T. E. Osterkamp, The role of snow cover in the warming of arctic permafrost, Geophys. Res. Lett., 30(13), 1721, doi:10.1029/2003GL017337, 2003.

Schimel, J. P., Bilbrough, C., & Welker, J. M. (2004). Increased snow depth affects microbial activity and nitrogen mineralization in two Arctic tundra communities. Soil Biology and Biochemistry, 36(2), 217-227.

Sjögersten, S., van der Wal, R., and Woodin, S. J. (2006). Small-scale hydrological variation determines landscape CO2 fluxes in the high Arctic. Biogeochemistry, 80(3), 205–216. doi:10.1007/s10533-006-9018-6.

Sturm, M., Schimel, J., Michaelson, G., Welker, J. M., Oberbauer, S. F., Liston, Fahnestock J. and Romanovsky, V. E. (2005). Winter biological processes could help convert arctic tundra to shrubland. Bioscience, 55(1), 17-26.

Tiuri, M. E., A. H. Sihvola, E. G. Nyfors, and M. T. Hallikaiken (1984), The complex dielectric constant of snow at microwave frequencies, Oceanic Engineering, IEEE Journal of, 9(5), 377–382, doi:10.1109/JOE.1984.1145645.

Wainwright, H. M., J. Chen, D. S. Sassen, and S. S. Hubbard (2014), Bayesian hierarchical approach and geophysical data sets for estimation of reactive facies over plume scales, Water Resour. Res., 50, 4564–4584, doi:10.1002/2013WR013842.

Wainwright, H. M., B. Dafflon, L. J. Smith,M. S. Ha hn, J. B. Curtis, Y. Wu, C. Ulrich, J.E. Peterson, M.S. Torn, and S.S. Hubbard (2015), Identifying multi scale zonation and assessing the relative importance of polygon geomorphology on carbon fluxes in an Arctic tundra ecosystem, J. Geophys. Res. Biogeosci., 120,788–808, doi:10.1002/2014JG002799.

Wainwright, H. M., A. Flores Orozco, M. Bücker, B. Dafflon, J. Chen, S. S. Hubbard, and K. H. Williams (2016), Hierarchical Bayesian method for mapping biogeochemical hot spots using induced polarization imaging, Water Resour. Res., 52, doi:10.1002/2015WR017763.

Wikle, C. K., R. F. Milliff, D. Nychka, and L. M. Berliner (2001), Spatiotemporal hierarchical Bayesian modeling: Tropical ocean surface winds, J. Am. Stat. Assoc., 96(454), 382–397.

Zhang, T. J. (2005). Influence of the seasonal snow cover on the ground thermal regime: An overview. Reviews of Geophysics 43: RG4002. doi:10.1029/2004RG000157.

Zona, D., D. A. Lipson, R. C. Zulueta, S. F. Oberbauer, and W. C. Oechel (2011), Microtopographic controls on ecosystem functioning in the Arctic Coastal Plain, *J. Geophys. Res. Biogeo.* (2005–2012), 116(G4).

Zona, D., Gioli, B., Commane, R., Lindaas, J., Wofsy, S. C., Miller, C. E., ... & Chang, R. Y. W. (2016). Cold season emissions dominate the Arctic tundra methane budget. Proceedings of the National Academy of Sciences, 113(1), 40-45.

The Cryosphere Discuss., doi:10.5194/tc-2016-168, 2016
Manuscript under review for journal The Cryosphere
Published: 30 August 2016

List of Figures

Figure 1. (a) Location of Barrow, Alaska, USA, and Barrow Environmental Observatory (BEO) from Hubbard et al. (2013). (b) NGEE-Arctic site with the digital elevation map from the airborne LiDAR (in meters). The black boxes are the intensive sampling plots (Plot A, B, C and D). The white rectangles are the fine-grid snow depth measurements by a point probe. The three black lines represent the transects.

Figure 2. Radar velocity as a function of (a) co-located snow depth measured by a point probe and (b) elevation difference (i.e., topographic variability) within 1 m. (c) Comparison between the probe-derived and GPR-derived snow depth at all the co-located locations (blue circles) and at selected locations (red circles) where topographic variability is low.

Figure 3. Elevation and snow depth in Plots A, B, C and D. The left column is LiDAR DEM (in meters), the middle column is the probe measured snow depth (in meters), and the right column is the interpolated snow depth estimated using GPR (in meters).

Figure 4. (a) UAS-derived DSM in meters (August, 2014), b) UAS-derived snow depth in meters (May, 2015), and (c) comparison between the UAS-based and probe-based snow depth at all the locations (blue circles) and at selected locations (red circles) having low topographic variability.

Figure 5. Boxplots of (a) snow depth and (b) elevation and (c) microtopographic elevation in Plots A-D.

The Cryosphere Discuss., doi:10.5194/tc-2016-168, 2016
Manuscript under review for journal The Cryosphere
Published: 30 August 2016

Figure 6. Correlation coefficients between snow depth and topographic metrics as a function of the wavelet scale: (a) the microtopographic elevation, and (b) the wind factor of macrotopography.

Figure 7. The estimated mean snow depth across the site (in meters) based on (a) the proposed Bayesian method including the correlation to microtopography, and (b) the kriging-based interpolation of the snow surface. The spatial extent is the same as Figure 1b.

Figure 8. The estimated standard deviation of snow depth across the site (in meters) based on (a) the proposed Bayesian method including the correlation to microtopography, and (b) the kriging-based interpolation of the snow surface. The spatial extent is the same as Figure 1b.

Figure 9. Estimated mean and confidence intervals from the Bayesian method, compared to the probe-measured snow depth by (a) using the correlation to microtopography and (b) interpolating the snow surface. The red circles represent the snow depth at the validation locations (the probe measurements not used in the estimation), the blue lines are the confidence intervals based on the standard deviation (STD) multiplied by 1.9 (94% confidence intervals), and the black lines are the one-to-one line.

The Cryosphere Discuss., doi:10.5194/tc-2016-168, 2016
Manuscript under review for journal The Cryosphere
Published: 30 August 2016

The Cryosphere Discussions
Open Access

List of Tables

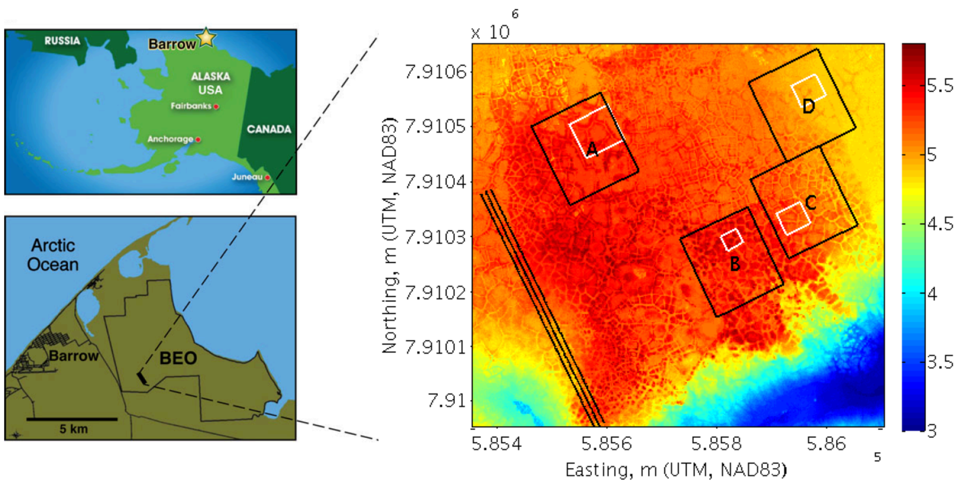

(a) (b)

Figure 1. (a) Location of Barrow, Alaska, USA, and Barrow Environmental Observatory (BEO) from Hubbard et al. (2013). (b) NGEE-Arctic site with the digital elevation map from the airborne LiDAR (in meters). The black boxes are the intensive sampling plots (Plot A, B, C and D). The white rectangles are the fine-grid snow depth measurements by a point probe. The three black lines represent the transects.

The Cryosphere Discuss., doi:10.5194/tc-2016-168, 2016
Manuscript under review for journal The Cryosphere
Published: 30 August 2016

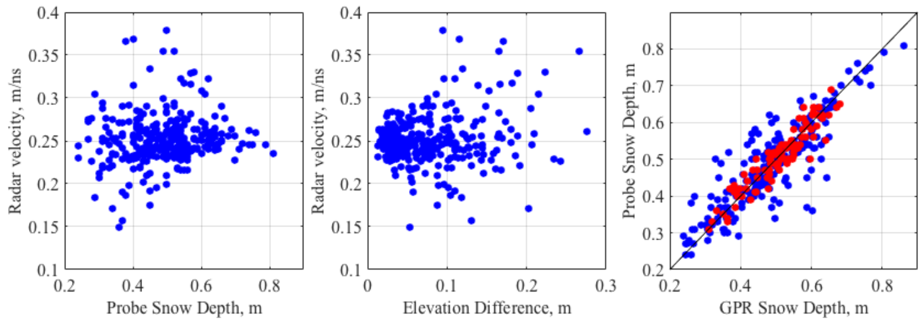

(a) (b) (c)

Figure 2. Radar velocity as a function of (a) co-located snow depth measured by a point probe and (b) elevation difference (i.e., topographic variability) within 1 m. (c) Comparison between the probe-derived and GPR-derived snow depth at all the co-located locations (blue circles) and at selected locations (red circles) where topographic variability is low.

The Cryosphere Discuss., doi:10.5194/tc-2016-168, 2016
Manuscript under review for journal The Cryosphere
Published: 30 August 2016

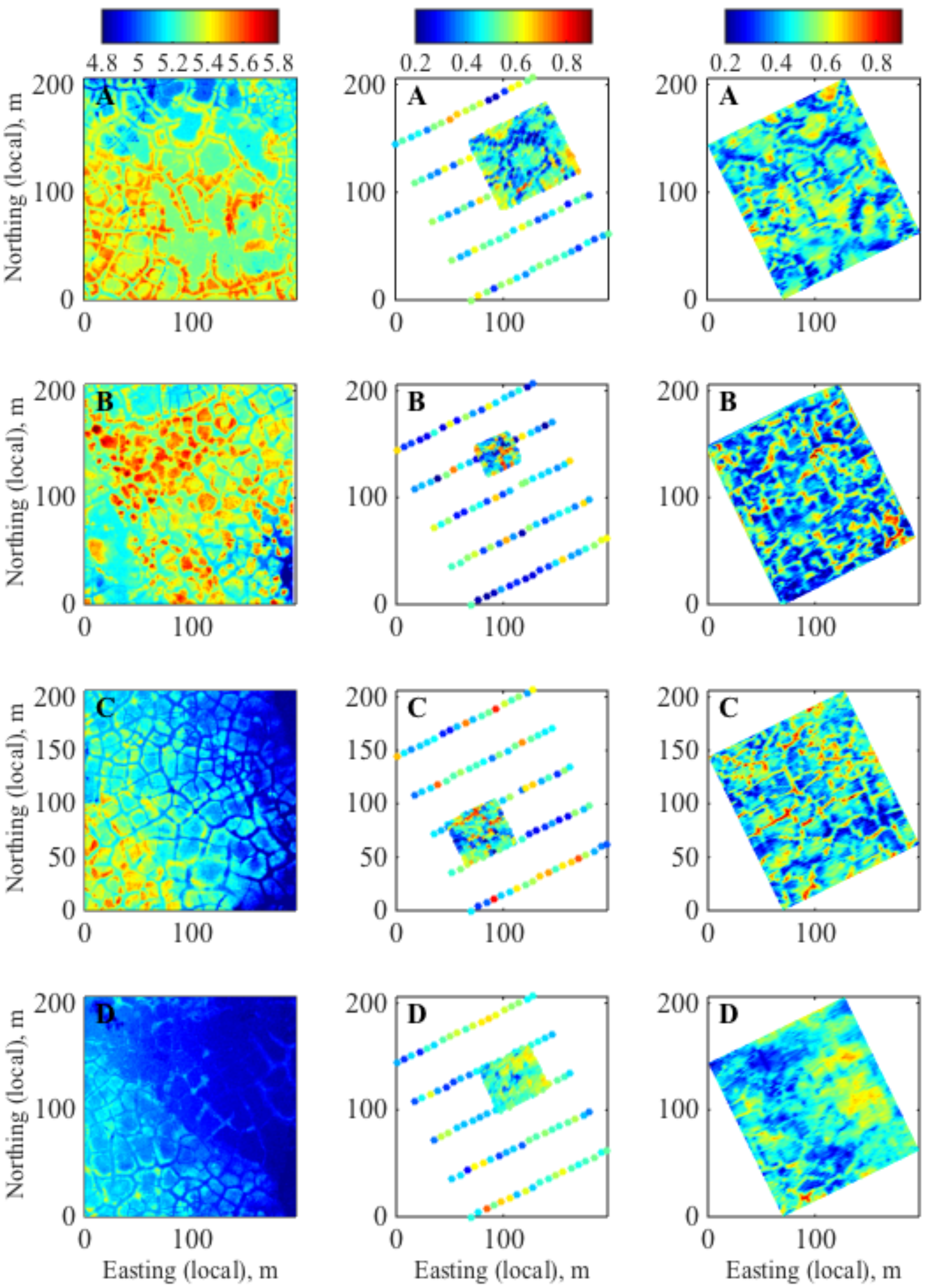

Figure 3. Elevation and snow depth in Plots A, B, C and D. The left column is LiDAR DEM (in meters), the middle column is the probe measured snow depth (in meters), and the right column is the interpolated snow depth estimated using GPR (in meters).

The Cryosphere Discuss., doi:10.5194/tc-2016-168, 2016
Manuscript under review for journal The Cryosphere
Published: 30 August 2016

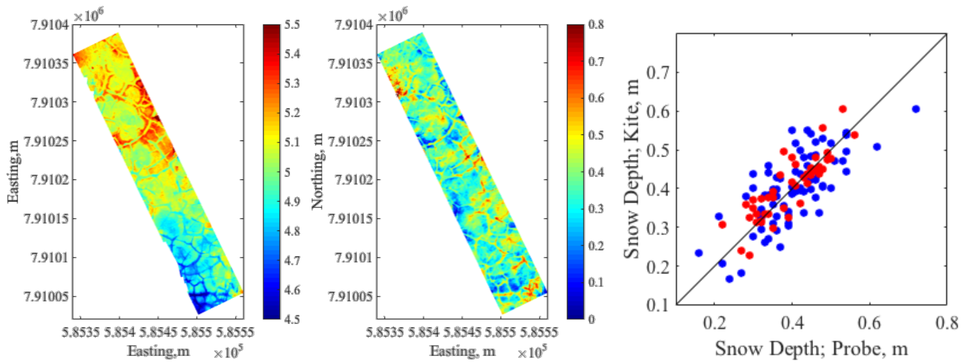

(a) (b) (c)

Figure 4. (a) UAS-derived DSM in meters (August, 2014), b) UAS-derived snow depth in meters (May, 2015), and (c) comparison between the UAS-based and probe-based snow depth at all the locations (blue circles) and at selected locations (red circles) having low topographic variability.

The Cryosphere Discuss., doi:10.5194/tc-2016-168, 2016
Manuscript under review for journal The Cryosphere
Published: 30 August 2016

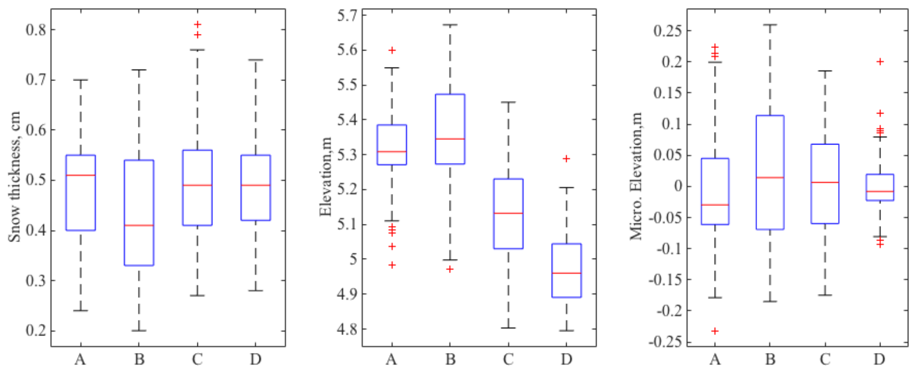

(a) (b) (c)

Figure 5. Boxplots of (a) snow depth and (b) elevation and (c) microtopographic elevation in Plots A-D.

The Cryosphere Discuss., doi:10.5194/tc-2016-168, 2016
Manuscript under review for journal The Cryosphere
Published: 30 August 2016

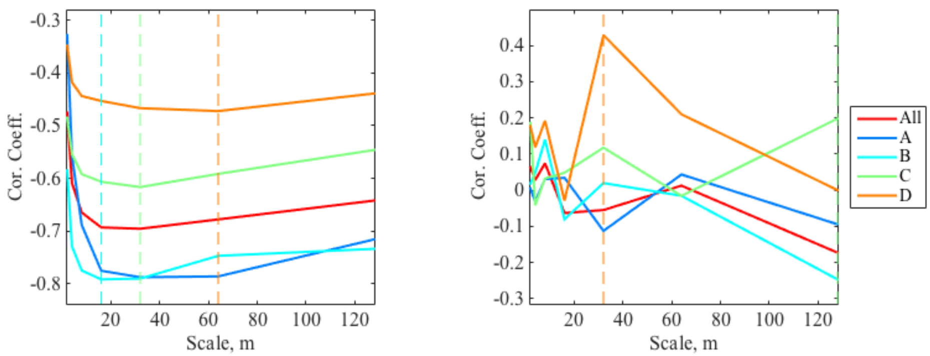

(a) (b)

Figure 6. Correlation coefficients between snow depth and topographic metrics as a function of the wavelet scale: (a) the microtopographic elevation, and (b) the wind factor of macrotopography.

The Cryosphere Discuss., doi:10.5194/tc-2016-168, 2016
Manuscript under review for journal The Cryosphere
Published: 30 August 2016

The Cryosphere Discussions

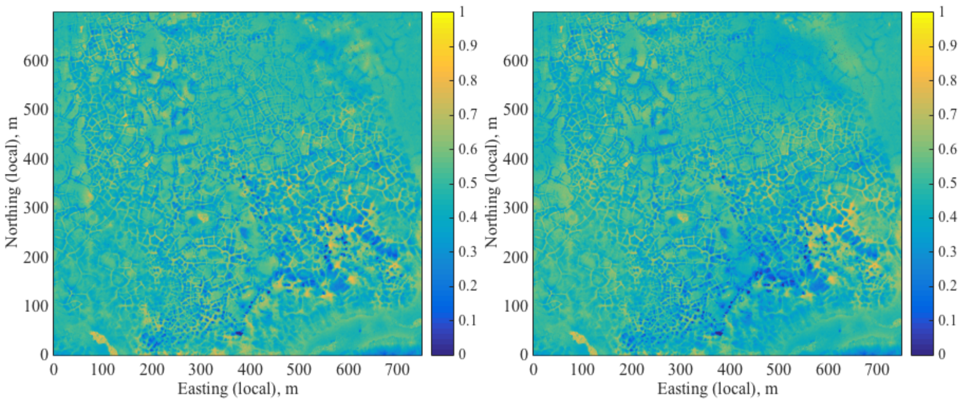

(a) (b)

Figure 7. The estimated mean snow depth across the site (in meters) based on (a) the proposed Bayesian method including the correlation to microtopography, and (b) the kriging-based interpolation of the snow surface. The spatial extent is the same as Figure 1b.

The Cryosphere Discuss., doi:10.5194/tc-2016-168, 2016
Manuscript under review for journal The Cryosphere
Published: 30 August 2016

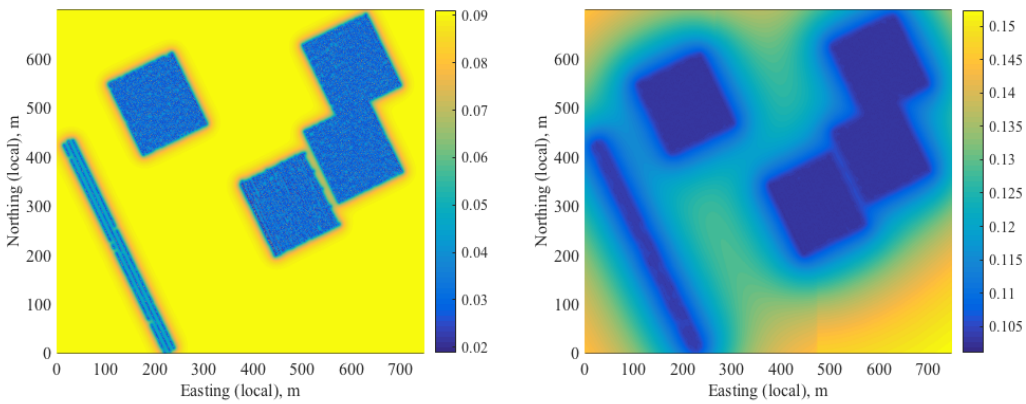

(a) (b)

Figure 8. The estimated standard deviation of snow depth across the site (in meters) based on (a) the proposed Bayesian method including the correlation to microtopography, and (b) the kriging-based interpolation of the snow surface. The spatial extent is the same as Figure 1b.

The Cryosphere Discuss., doi:10.5194/tc-2016-168, 2016
Manuscript under review for journal The Cryosphere
Published: 30 August 2016

The Cryosphere
Discussions
Open Access

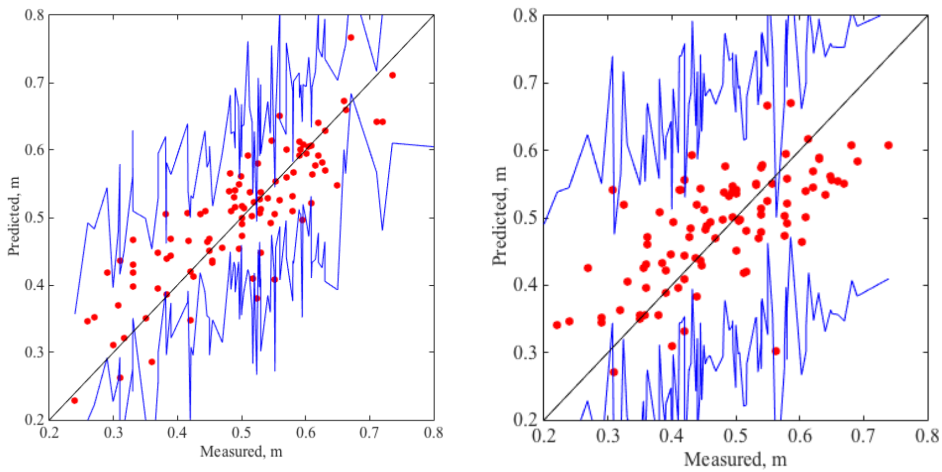

(a) (b)

Figure 9. Estimated mean and confidence intervals from the Bayesian method, compared to the probe-measured snow depth by (a) using the correlation to microtopography and (b) interpolating the snow surface. The red circles represent the snow depth at the validation locations (the probe measurements not used in the estimation), the blue lines are the confidence intervals based on the standard deviation (STD) multiplied by 1.9 (94% confidence intervals), and the black lines are the one-to-one line.

The Cryosphere Discuss., doi:10.5194/tc-2016-168, 2016
Manuscript under review for journal The Cryosphere
Published: 30 August 2016

The Cryosphere
Discussions
Open Access

Table 1. Multivariate normal distribution defined for each variable.

Variable		Type	Distribution	Covariance	Mean vector
Snow depth	$\boldsymbol{y}$	Process model	$p(\boldsymbol{y}\|\boldsymbol{a}, z_d)$	Σ	$\mathrm{A}\boldsymbol{a}$
Probe data	z_p	Data model	$p(z_p\|\boldsymbol{y})$	D_p	$\boldsymbol{y}$
GPR data	z_g	Data model	$p(z_g\|\boldsymbol{y}, \boldsymbol{b})$	D_g	$\mathrm{B}\boldsymbol{y} + b_0$
Snow-depth parameters	$\boldsymbol{a}$	Prior	$p(\boldsymbol{a})$	$\mathrm{V}_{\boldsymbol{a}}$	$\boldsymbol{\mu}_{\boldsymbol{a}}$
GPR parameters	$\boldsymbol{b}$	Prior	$p(\boldsymbol{b})$	$\mathrm{V}_{\boldsymbol{b}}$	$\boldsymbol{\mu}_{\boldsymbol{b}}$

The Cryosphere Discuss., doi:10.5194/tc-2016-168, 2016
Manuscript under review for journal The Cryosphere
Published: 30 August 2016

Table 2. Root mean squared error (RMSE) between the UAS-derived DSM and GPS elevation measurements based on the three schemes: nearest neighbor, average, and minimum elevation within the 0.5 m radius.

	Nearest (cm)	Average (cm)	Minimum (cm)
July 2013	6.88	6.41	6.62
August 2014	6.40	6.19	6.34

The Cryosphere Discuss., doi:10.5194/tc-2016-168, 2016
Manuscript under review for journal The Cryosphere
Published: 30 August 2016

Table 3. *p* values from Tukey's pairwise comparison test for each pair of the plots.

	Snow depth
Plot A – Plot B	**6.34×10^{-3}**
Plot A – Plot C	0.982
Plot A – Plot D	0.998
Plot B – Plot C	**1.72×10^{-3}**
Plot B – Plot D	**3.55×10^{-3}**
Plot C – Plot D	0.997

The Cryosphere Discuss., doi:10.5194/tc-2016-168, 2016
Manuscript under review for journal The Cryosphere
Published: 30 August 2016

Table 4. Estimated geostatistical parameters and covariance models for snow depth, snow surface and residual snow depth.

	Model	Range (m)	Variance (m^2)	Nugget Ratio
Snow depth	Exponential	12.3	1.6×10^{-2}	0.0
Snow surface	Spherical	253.3	2.0×10^{-2}	0.16
Residual snow depth	Exponential	15.0	8.3×10^{-3}	0.0

The Cryosphere Discuss., doi:10.5194/tc-2016-168, 2016
Manuscript under review for journal The Cryosphere
Published: 30 August 2016

Table A.1. Posterior distributions during the Gibbs sampling

Variable		Covariance, Q	Mean vector
Snow depth	$\boldsymbol{y}$	$(B^T D_g^{-1} B + D_p^{-1} + \Sigma^{-1})^{-1}$	$Q(B^T D_g^{-1}(z_g - b_0) + D_p^{-1} z_p + \Sigma^{-1} A\boldsymbol{a})$
Snow depth parameters	$\boldsymbol{a}$	$(A^T \Sigma^{-1} A + V_a^{-1})^{-1}$	$Q(A^T \Sigma^{-1} \boldsymbol{y} + V_a^{-1} \boldsymbol{\mu}_a)$
GPR parameters	$\boldsymbol{b}$	$(H^T D_g^{-1} H + V_b^{-1})^{-1}$	$Q(B^T D_g^{-1} (z_g - b_0) + V_b^{-1} \boldsymbol{\mu}_b)$